Research article

A study of the structural, morphological, and optical properties of shock treated SnO₂ nanoparticles: removal of Victoria blue dye

M. Jarvin [a], S.S.R. Inbanathan [a,*], D. Rani Rosaline [b], A. Josephine Prabha [c], S.A. Martin Britto Dhas [d]

[a] Post Graduate and Research Department of Physics, The American College, Madurai, 625002, Tamil Nadu, India
[b] Post Graduate and Research Department of Chemistry, Lady Doak College, Madurai, 625002, Tamil Nadu, India
[c] Department of Physics, Bishop Heber College, Tiruchirappalli, 620017, Tamil Nadu, India
[d] Shock Wave Research Laboratory, Department of Physics, Abdul Kalam Research Center, Sacred Heart College, Tirupattur, Vellore, 635 601, Tamil Nadu, India

A B S T R A C T

In this work, Tin Oxide (SnO₂) nanoparticles (NPs) were prepared by green microwave followed by hydrothermal methods, using tea extract as a reducing agent. To verify the stability of physical and chemical properties of SnO₂ NPs, samples were subjected to shock impulsion experimentation. Different characterization techniques were employed to analyze the crystallinity, molecular structure, and optical parameters of the control SnO₂ and shock wave exposed SnO₂ NPs. Powder X-ray diffraction (PXRD) revealed no significant change in crystal structure. Williamson – Hall analysis demonstrates that the stress and strain between Sn–O changes during the impulsion of shocks. Rietveld analysis reveals change in the bond length between Sn–O. The molecular structure is not affected during shock loading, but the optical properties do change. From the photocatalytic experiment, we find that the parameters such as stress, strain, and bond length make an enormous impact in photocatalytic application.

1. Introduction

One of the major drawbacks observed in the textile and color industry is the removal of colors (dyes) from wastewater. There are different types of dyes, including organic, inorganic, and azo. The color and other properties of dye are determined by chemical structure, and divided into anionic and cationic dyes [1, 2, 3]. Among the cationic dyes, Victoria blue (VB) is widely utilized as a bright coloring agent in various industries, including wool, silk, nylon, and acrylics with a molecular weight of 506.08. It has the same functional group as onium groups and N⁺ ions, and exhibits excitation wavelengths of 610 nm [4]. VB dye contains cationic functional groups that can dissociate into positively charged ions in a water solution. The use of metal oxides to break chemical bonds in the VB dye has stimulated significant research in recent years. There are several metal oxides used as catalysts. Among the several catalysts, Tin oxide (SnO₂) is considered to be the most effective for eliminating hazardous dye from the wastewater via photon energy [5, 6, 7, 8, 9, 10]. It is also used for other applications such as photocatalytic, electrochemical, and sensing. Tin oxide is widely used for photocatalytic applications because of its ability to remove the cationic dye through electrostatic

attraction between VB dyes with SnO₂ NPs [11]. Tin (iv) oxide appears as white or off-white crystalline solid or powder, with a melting point of 1127 °C, and density of 6.95 g/cm³ at room temperature. SnO is a versatile intermediate to metallic Sn, Sn₃O₄, and SnO₂ the thermodynamically unstable nature of Sn (IV). Therefore it is relatively difficult to grow SnO single-crystals [12, 13]. Generally, SnO₂ possesses excellent electrical, optical, catalytic, and thermal properties. Numerous methods to synthesize SnO₂ NPs, including hydrothermal [14, 15], microwave oven [16, 17], sol-gel [18, 19, 20], co-precipitation [21, 22], solid-state [23, 24], and green methods [25, 26, 27, 28, 29] have been used to obtain SnO₂ NPs. Each method has both advantages and disadvantages. In the present study, the SnO₂ NPS were synthesized by microwave radiation followed by a hydrothermal method using tea extract as a reducing agent. The entire reaction took place in a compressed liquid environment. In the microwave method, microwave radiation is used as a heat source. The advantage of this method is that it is eco-friendly, cost effective and easy to synthesize. Moreover, there is no need for any chemical reducing agents because tea extract itself acts as a reducing agent. The combination of these methods effectively produces NPs with controlled shape and particle size [30, 31, 32]. Stability of the material's property is also

* Corresponding author.
E-mail address: stepheninbanathan@gmail.com (S.S.R. Inbanathan).

crucial for the device fabrication and photocatalytic application. For that, extreme pressure is applied to the material in the form of shockwaves. During the shock treatment, the material changes such physical properties as its grain size, phase, electronic state, morphology and oxidation state [33, 34]. Research reports are readily available on shock treated metal oxides such as ZnO [35], TiO$_2$ [36], AgO [37], NiO [38]. Based on the recent reports [39, 40] bulk SnO$_2$ is rutile in structure, tetragonal symmetry of *P4/mnm* space group at ambient pressure and temperature. At the pressure of 11.8 GPa, the rutile structure becomes CaCl$_2$ type structure of orthorhombic symmetry of the Pnnm space group. Material changes its phase into α-PbO$_2$, orthorhombic symmetry of the Pbcn space group at 12 GPa *(Pnnm to Pbcn)*. Pyrite FeS$_2$ structure cubic symmetry of *Pa-3* space group transformation occurs at the pressure of 25 Gpa. For SnO$_2$, tetragonal structure remains stable up to 18 GPa for 8 nm grain size nanoparticles. Above that pressure, the phase changes from tetragonal to cubic with the discontinuity in the volume.

Therefore, we undertook an investigation of SnO$_2$ NPs prepared by a green microwave-assisted hydrothermal method. We examined the prepared SnO$_2$ NPs exposed to different numbers of shock pulses (50, 100, and 150) and scrutinized its structural, molecular, and optical stabilities. The control SnO$_2$ and shock exposed SnO$_2$ NPs were also explored for photocatalytic application under UV light for the removal of VB dye as a model pollutant.

2. Experimental details

2.1. Materials used

For the synthesis of SnO$_2$ nanoparticles, SnCl$_2$. 2H$_2$O (Stannous chloride) was used as a precursor material, analytical grade purchased from Merck (India). The green tea bags (*camellia sinensis*) were procured from a commercial tea vendor (Tajmahal, India). For all experiments, double deionized water was used.

2.2. Synthesis of SnO$_2$ nanoparticles

SnO$_2$ NPs were synthesized by microwave heating followed by a hydrothermal route. To accomplish the synthesis, after the 60 ml DI water reached the boiling temperature, 2 g of tea were boiled for 2 min. The resultant 50 ml dark brown color solution was cooled to room temperature and filtered through filter paper (pore size of 10 μm), and the filtered tea extract was used for SnO$_2$ NPs preparation. 0.1 M of SnCl$_2$. 2H$_2$O was mixed with 50 ml of green tea extract and sonicated in the solution for 30 min (power 50 W, frequency 40 kHz) at room temperature. Once the solution was sufficiently mixed, the mixture was irradiated in a domestic microwave for 3 min at the power of 700 W at the frequency of 2450 Hz. Subsequently, the colloidal mixture was transferred into a stainless steel autoclave. The hydrothermal reaction was executed at 180 °C for 24 h. The powder was collected, and then triple cleansed of excess chloride ions by means of ethanol mixed in DI water. The sample was annealed at 300 °C for 4 h. During the annealing process, SnO$_2$ NPs were formed through the oxidation of Sn^0.

2.3. SnO$_2$ NPs formation mechanism

In SnO$_2$ NPs formation, tea extract functions both as capping and a reducing agent. Tea extract contains the potassium metal present in the large amount of 92–151 mg/l and other metals such as sodium (35–69 mg/l), calcium (1.9–3.5 mg/l), fluoride (0.8–2.0 mg/l), aluminum (1.0–2.2 mg/l), manganese (0.52–1.9 mg/l), and iron (0.020–0.128 mg/l). Tea extract contains polyphenols which also acts as an antioxidant. This phenolic group contains four flavonoid groups, including epicatechin gallate (ECG) (203–471 mg/l), epigallocatechin gallate (EGCG) (117–442 mg/l), epicatechin (EC) (25–81 mg/l), and epigallocatechin (EGC) (16.9–150 mg/l) [41]. In the first step, SnCl$_2$. 2H$_2$O is converted into Sn^0 in sonication (Eqs. (1), (2)), and microwave process by means of

epigallocatechin (EGC) in the phenolic group. –OH is the major group in epigallocatechin (EGC) in the reduction process [42]. During the hydrothermal process, the reduced Sn particles develop into a well-defined structure.

$$SnCl_2 + H_2O \rightarrow Sn^{2+} + 2HCl \tag{1}$$

$$Sn^{2+} + OH \rightarrow Sn^0 \tag{2}$$

The second step is the phase changing process. By means of aerial oxidation (Eq. (3)) during the annealing process, Sn transforms into SnO$_2$ NPs.

$$Sn^0 + heat\ process \rightarrow SnO_2 \tag{3}$$

2.4. Photo degradation experiment

The photo degradation process of control SnO$_2$ and shock exposed SnO$_2$ NPs were examined under UV illumination. Victoria blue (VB) dye was employed as a model pollutant. To achieve an adsorption-desorption process between the SnO$_2$ NPs and the VB dye, a solution of 5 ppm (5 mg/L) VB dye and a substantial quantity of photocatalyst were magnetically stirred in a Pyrex glass vessel at dark conditions for 20 min. The UV light was placed above the solution. The distance between the UV light and the solution was approximately 10 cm. The specification of UV light was 8 W, 365 nm, UV light. The temperature maintained throughout the entire experiment was between 28-32 °C. At the conclusion of the adsorption process, the UV light was illuminated. At appropriate intervals, .5 ml of aliquots were collected. The collected aliquots were centrifuged to extract the particles. Collected aliquots concentrations were measured via UV-Visible absorbance spectrophotometer at the maximum absorption $\lambda_{max} = 610$ nm. The degradation efficiency of VB dye was defined as follows (Eq. (4)),

$$Degradation\ efficiency\ (\%) = \frac{C_0 - C}{C_0} \times 100 \tag{4}$$

where C_0, VB dye initial concentration and C is the concentration at different reaction times (min).

2.5. Kinetics study

For the determination of the rate of VB dye degradation, first and second-order kinetics were applied. The rate of decolorization of control SnO$_2$ and shock treated individual SnO$_2$ NPs was discerned by applying pseudo-first and second-order kinetic models.

First order kinetic model is expressed as (Eq. (5)) [37, 43],

$$\ln(C_0 / C_t) = k_1 t \tag{5}$$

Second order kinetic model is expressed as (Eq. (6)),

$$1 / C_t - 1/C_0 = k_2 t \tag{6}$$

where C_0 is the initial absorbance or concentration value of VB dye, C_t concentration at a given time't', rate constants for first and second-order are k_1 and k_2. The correlation coefficient (r^2) is obtained by the plot of first and second-order reaction graphs. For the first order, the graph plots between $\ln(C_0/C_t)$ vs time, for the second-order $1/C_t$-$1/C_0$ vs time.

2.6. Shock wave loading

The powder samples were placed in a 10 × 10 × 2 mm^3 polyethylene sample cell. A table top pressure driven Reddy tube generated shock waves at 1.7 Mach number with a transient pressure, and temperature of 0.857 MPa, and 594 K, respectively. Subsequently, shock pulses (50, 100, 150 counts) were exposed sequentially at timed intervals of 5 s.
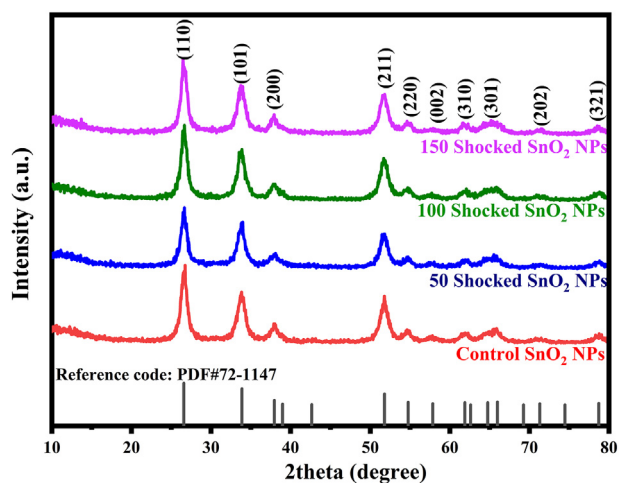
Figure 1. XRD pattern of control SnO2 and shock exposed SnO2 NPs.

2.7. Material characterization

Powder X-ray diffraction (PXRD) analysis was done with an Ultima III max (Rigaku) X-ray diffractometer with Cu-Ka ($\lambda = 1.5418$ Å) radiation in the range 20°-80° at grazing angle 1°, and step size 0.01 deg. Fourier transform infrared spectrophotometer (Jasco FT/IR-4600) identified the functional groups of the samples. KBr was used to prepare the sample in the pellet form for FTIR analysis. Microscopic images were captured by Field emission scanning electron microscope (FESEM), using a SIGMA HV – Carl Zeiss apparatus. Photoluminescence (PL) properties of the samples were recorded by a spectrofluorometer (JASCO FP-8300). UV-vis diffuse reflectance spectroscopy (SHIMADZU/UV2600) was employed to obtain data on the synthesized samples, such as absorption spectrum and band gap energy.

3. Results and discussion

3.1. XRD

Structural stability, purity, and grain size of the control SnO$_2$ and shock loaded SnO$_2$ NPs were identified by using a powder X-ray diffractometer (PXRD). Figure 1 Shows the XRD pattern of control SnO$_2$ and shocked SnO$_2$ NPs. All the XRD patterns accurately correspond to JCPDS card 72–1147 with a space group of *P42/mnm*. Moreover, the observed intensity peaks belong to the tetragonal structure. The intensity peaks of SnO$_2$ at the 2θ range are 26.9, 33.9, 52.2, and 65 belong to the hkl planes of (110), (101), (211), and (112). The grain size of the control SnO$_2$ and shock exposed SnO$_2$ NPs was calculated via Debye-Scherer's formula.

The control SnO$_2$ NPs reveals an average grain size of 11.71 nm. Shock loaded samples were compared with control SnO$_2$ samples to find the structural stability. When the shock wave was applied to the samples, no new peaks appeared nor did any change occur in the existing peaks. This result clearly demonstrates that SnO$_2$ did not alter or change phase when the samples were impacted by an impulsion of 150 shocks. The intensity of the peak did not change, which demonstrates stability in nature. When the number of shocks (50,100 and 150) increases, the grain size is also found to increase (14.92, 14.36, and 18.22 nm). This may be due to the dynamic recrystallization that occurs during the explosion of shock treatment, i.e fusion of grains [38, 44]. As per the report [35], the NPs with lower grain sizes have better stability than those possessing higher grain sizes.

The Rietveld refinement was performed using the FULLProf-suite software for the measured powder X-ray diffraction data of control SnO$_2$ and shock loaded samples. The samples exhibited the same tetragonal structure even at shocking conditions, shown in Figure 2. The stability of the material is primarily based on the orientation of the crystal, atomic position, grains, and the bond length between Sn–O. During shock treatment the minute change in the bond length between the Sn–O occurs but the orientation of the crystal does not alter. As per
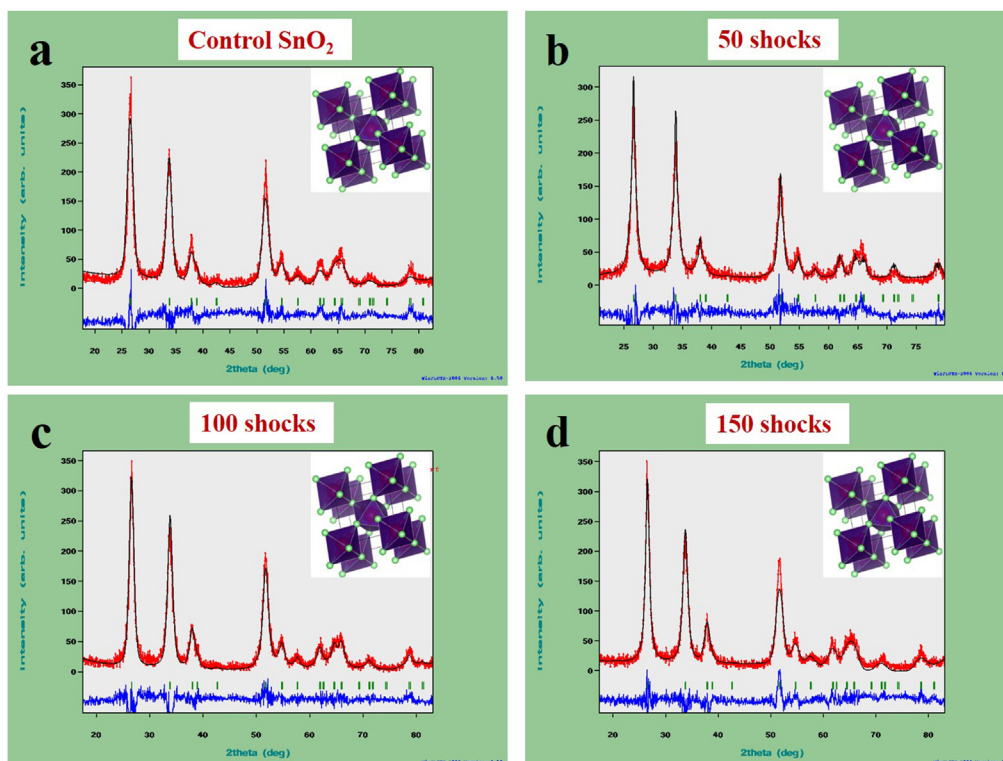

Figure 2. The Rietveld refinement of (a) control SnO$_2$ (b) 50, (c) 100 and (d) 150 shock exposed SnO$_2$ NPs.

Table 1. Profile refinement parameters of control SnO$_2$ and shock exposed SnO$_2$ NPs.

samples	control SnO$_2$	50 Shock	100 Shock	150 Shock
Crystal system	Tetragonal	Tetragonal	Tetragonal	Tetragonal
Space group	P 42/mnm(136)	P 42/mnm(136)	P 42/mnm(136)	P 42/mnm(136)
Lattice parameter(Å)				
a = b≠c	4.73700 and 3.18500	4.73700 and 3.18500	4.73700 and 3.18500	4.73700 and 3.18500
α = β = γ	90.0000	90.0000	90.0000	90.0000
Unit cell volume(Å)	72.844	71.707	71.791	72.131
Atomic coordinates				
Sn				
X	0.0000	0.0000	0.0000	0.0000
Y	0.0000	0.0000	0.0000	0.0000
Z	0.0000	0.0000	0.0000	0.0000
Occupancy	2.10290	0.63608	0.53304	3.71841
O				
X	0.30278	0.28659	0.29856	0.29619
Y	0.30278	0.28659	0.29856	0.29619
Z	0.0000	0.0000	0.0000	0.0000
Occupancy	0.89800	11.3799	1.10646	0.49639
Bond length (Sn– O)Å	2.21	2.27	2.23	2.24
Refinement parameters				
R$_P$	25.5	32.9	20.2	32.1
R$_{WP}$	32.8	39.9	26.4	39.1
R$_{EXP}$	19.6	26.9	19.4	22.6
χ^2	4.39	2.19	1.85	3.000
R$_{Bragg}$	16.5	14.8	7.33	11.1
R$_F$	7.56	14.8	4.49	10.4
X-ray density(g/cm^3)	7.00	7.00	7.00	7.00

the literature report, only beyond 18 GPa the 8 nm SnO$_2$ sample changes its tetragonal symmetry to cubic [39]. This provides clear evidence for the high mechanical stability and high shockwave resistance nature of SnO$_2$ compared with TiO$_2$ metal oxide nanoparticles which undergo phase transition while shock loaded condition [36]. By using pseudo-Voigt profile function, the Le Bail refinement parameters, such as the correct fit, are denoted by χ2, R factors (RP = profile factor, RB = Bragg factor, and RF = crystallographic factor). Occupancy gives the details about the number of atoms in a unit cell of Sn and O, atomic coordinates of Sn and O, the volume of the cell (V), and lattice constant parameters (a, b, c).All four samples were calculated, and obtained the particular profile refinement parameters listed in Table (1).

3.2. Williamson –Hall method

3.2.1. Uniform deformation model (UDM)

Defect and distortion in the crystalline powder create the stain in the NPs structure. Any crystalline change that occurs during the impact of shock can be analyzed in the Uniform deformation model. Strain-induced line broadening β. Crystallite size from Scherer's formula also yields information about line broadening (1/cosθ). The total line broadening is obtained when adding Strain-induced line broadening with crystallite size [45]. The Uniform deformation model (UDM) is isotropic. Therefore, the strain in the crystal is uniform in all crystallographic directions. Figure 3 gives the lot the graph between 4sinθ vs βcosθ. 4sinθ and βcosθ. The Y intercept of the plot gives the crystallite size and the slope of the plot gives strain value.

3.2.2. Uniform stress deformation model (USDM)

Particle elasticity and the crystal have a very low strain, making it impossible to calculate the crystal parameters directly. However, it can be calculated by using Hooke's law. Generally, Hooke's law reveals the relationship between stress (σ) and strain (ε), where E is the young's modulus or modulus elasticity. Young's modulus is different for different structures, for tetragonal structure young's modulus equation gives in [45]. S$_{ij}$ are elastic compliance for the tetragonal structure S11 = 7.426, S12 = −4.408, S13 = 1.0438, S33 = 2.946, S44 = 9.7 and S66 = 4.8216. In the USDM model stress is anisotropic. By plotting the graph between 4sinθ/E (X-axis) versus βcosθ (Y-axis) shown in Figure 4, the slope of the straight line gives the stress value (σ) and the Y-intercept gives the crystallite size.

3.2.3. Uniform deformation energy density model (UDEDM)

The UDEDM model also discloses the anisotropic behavior of the crystal; however, in some cases, the presumption is not confirmed. Therefore, the energy density is calculated based on Hooke's law. Figure 5 depicts the graph plotted between 4sinθ (2/E)$^{1/2}$ and βcosθ. The slope of the straight line gives the stress value (σ) and the Y-intercept gives the crystallite size. Negative slope designates compression of lattice [46, 47]. In the literature report, negative slope most often occurs with particles of smaller crystal size, whereas the positive slope is caused by the lattice expansion or tensile strain of the NPs [46, 47]. The summary of the W–H plot results tabulated in Table (2).

3.3. FTIR

The presence of functional groups, identification of unknown samples, and chemical bonding of the samples were analyzed by using FTIR analysis. Figure (6a) shows the FTIR spectrum of tea extract. The graph shows a wide absorption band at 3310 cm^{-1} due to the OH functional group in alcohols and phenolic compounds. Another intense peak at the 1628 cm^{-1} range indicates C=O polyphenol stretching and C=C stretching in the aromatic ring [48]. The control SnO$_2$ and 50, 100, 150 shocks treated SnO$_2$ NPs is shown in Figure (6b). The FTIR spectrum reveals absorption peaks in the same region for all three samples (50, 100, 150 shock), and no peak shifting or vanishing, nor emerging of new peaks, even after the impulsion of 150 shocks. The broad absorption band at 3431 cm^{-1} and 1637 cm^{-1} is due to the vibration of absorbed water molecules on the surface of the sample. The most important peak for SnO$_2$ NPs in the range of 632 cm^{-1} is the vibration of the asymmetric stretching of Sn–O [49, 50, 51]. This peak, which was exhibited in all the samples, indicates SnO$_2$ has higher molecular stability. For control SnO$_2$ NPs shows one intense peak at the range of 1160 cm^{-1} in the FTIR spectra may be assigned to a vibration of hydroxyl–tin bonds (Sn–OH) of different organic types of surface hydroxyl groups [50]. This peak disappeared for the shock exposed nanoparticles. Vanishing of peak (1160 cm^{-1}) and decreasing intensity peak (3431 cm^{-1}) indicates that hydroxyl radical was greatly affected due to the explosion of shock wave.

3.4. FESEM

Figure 7 depicts shock exposed and controlled SnO$_2$ NPs show the same structure with nearly the same particle size. All the NPs exhibit a small granular structure, above that small ball like SnO$_2$ nano crystalloaded it. The control SnO$_2$ NPs show a grain size of 30 nm. From the figure it is clear that there is no change in the morphology or size.

3.5. UV-vis spectroscopy

The optical property of shock-loaded and controlled SnO$_2$ NPs was characterized by using UV-Visible spectroscopy. Figure (8a) shows the UV absorption and (8b) Tauc plot of the control SnO$_2$ and shock loaded SnO$_2$ NPs. The control SnO$_2$ NPs shows the high absorption and broad peak at the region of 370 nm, which appropriately corresponds to
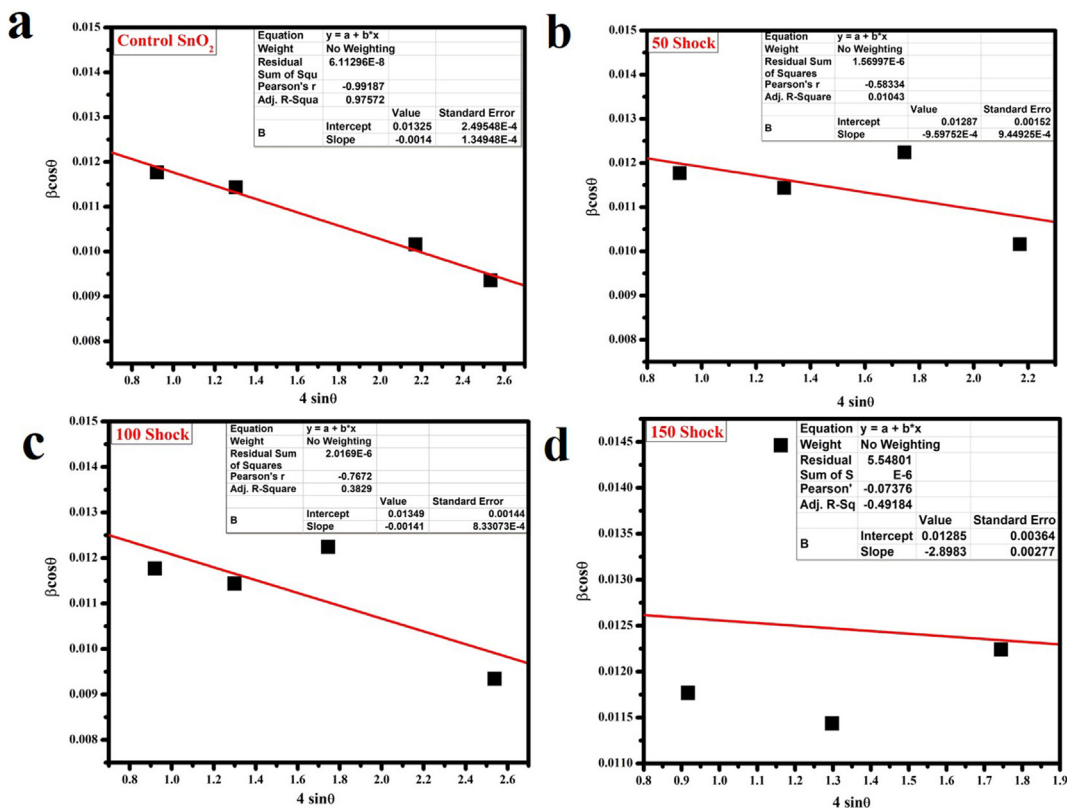
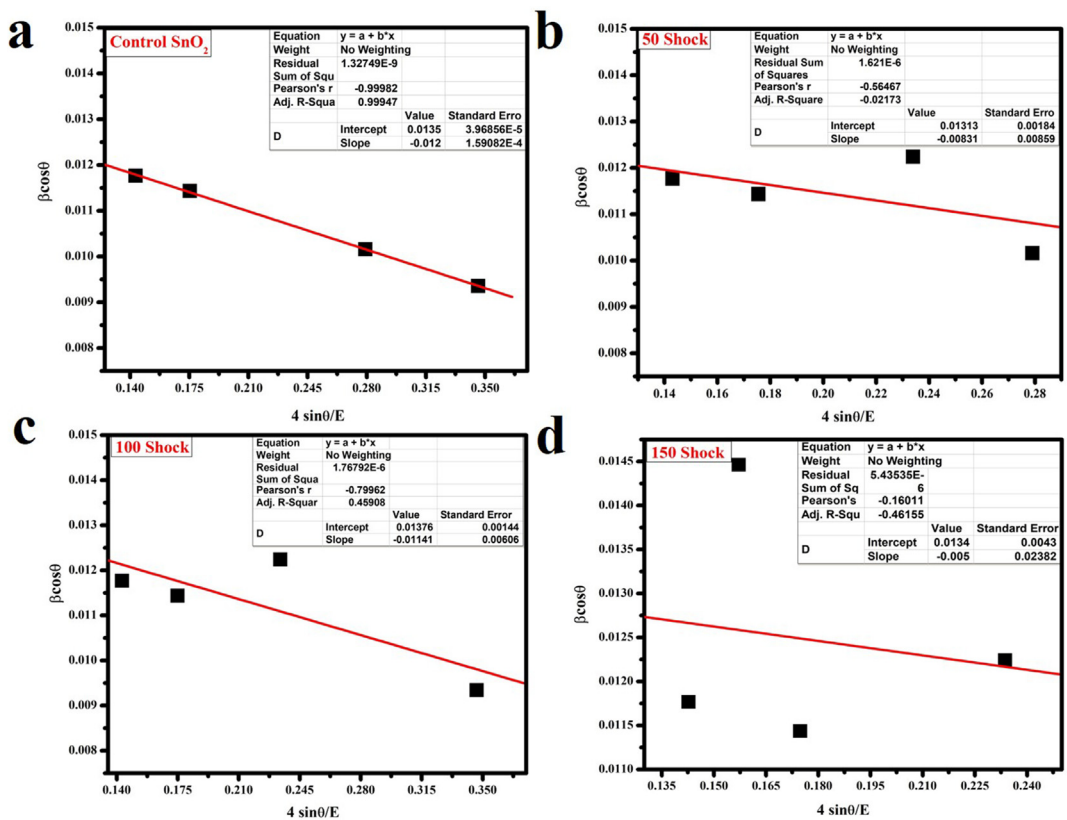**Figure 3.** UDM plot of (a) control SnO$_2$ (b) 50, (c) 100 and (d) 150 shock exposed SnO$_2$ NPs.

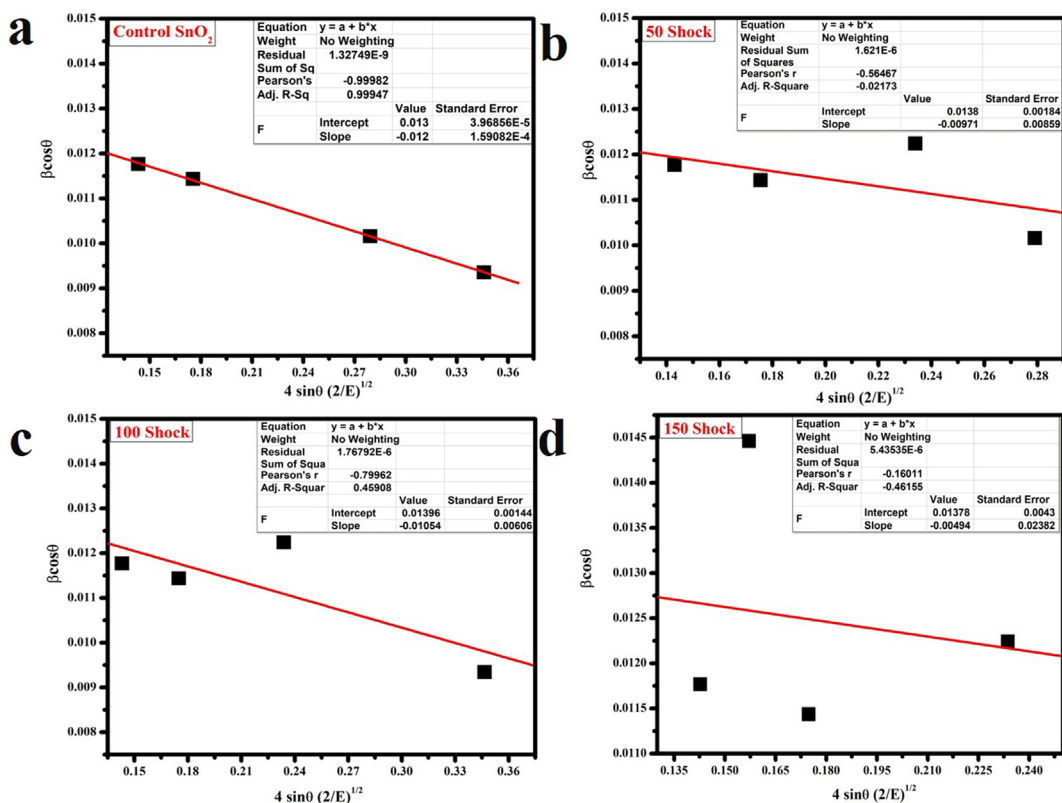**Figure 4.** USDM plot of (a) control SnO$_2$ (b) 50, (c) 100 and (d) 150 shock exposed SnO$_2$ NPs.

Figure 5. UDEDM plot of (a) control SnO$_2$ (b) 50, (c) 100 and (d) 150 shock exposed SnO$_2$ NPs.

Table 2. W–H report of control SnO$_2$ and shock exposed SnO$_2$ NPs.

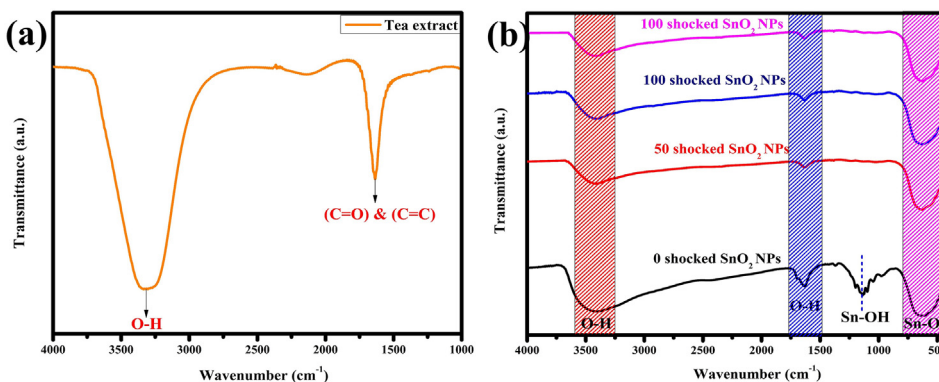| Sr.No	Samples	Scherrer method D(nm)	Williamson–Hall method								
			UDM		USDM			UDEDM			
			$\epsilon \times 10^{-3}$	D (nm)	σ (GPa)	$\epsilon \times 10^{-3}$	D (nm)	U (GPa)	σ (GPa)	$\epsilon \times 10^{-3}$	D (nm)
1.	control SnO$_2$	11.71	1.49	13.25	12.32	1.6555	13.51	12.27	38.67	1.342	13.75
2.	50- Shock	14.92	0.9597	12.87	8.31	1.1446	13.13	9.71	25.65	1.193	13.8
3.	100- Shock	13.36	1.41	13.49	11.41	1.5933	13.76	10.54	38.62	1.2962	13.96
4.	150- Shock	18.22	0.9358	12.85	8.16	1.1102	13.44	8.94	24.78	1.074	13.78

Figure 6. Shows the FTIR spectrum of (a) tea extract and (b) control SnO$_2$ and shock exposed SnO$_2$ NPs.

previously reported values [51, 52, 53, 54]. The broad and high absorption peak is due to the distribution and low crystallite size of the SnO$_2$ NPs. At the same time 50, 100, 150 shocks treated SnO$_2$ NPs shows the absorption in the same wavelength region (370–371 nm) only the change in the absorption intensity and the peak will sharpen. This is due to the defects created in the crystal structure during the impact of shocks. These defects and increasing crystal size diminish them and sharpen the absorption peaks [55]. There is no shift in the peaks; either red shift or blue shift occurs. All the peaks appear within the region of 370–371 nm. The sharp and broad absorption edge affects the Bandgap of the material.
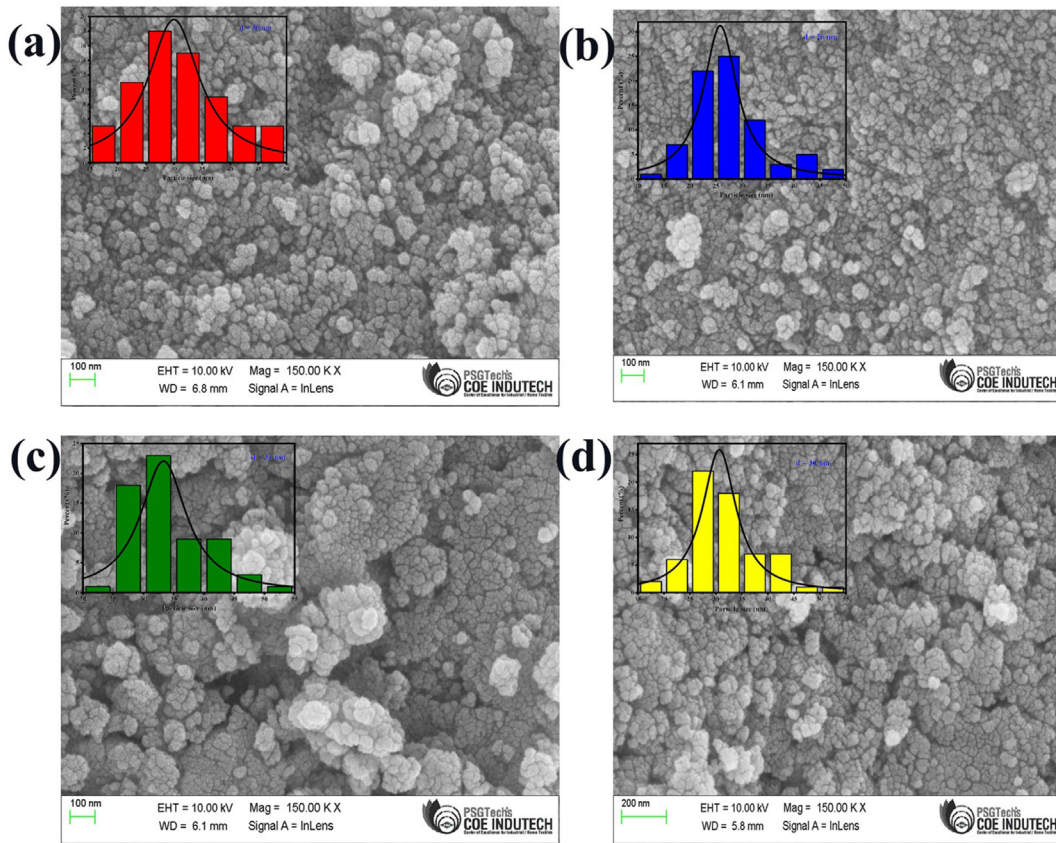
Figure 7. FESEM image of (a) control SnO$_2$ and (b) 50, (c) 100, and (d) 150 shock exposed SnO$_2$ NPs.
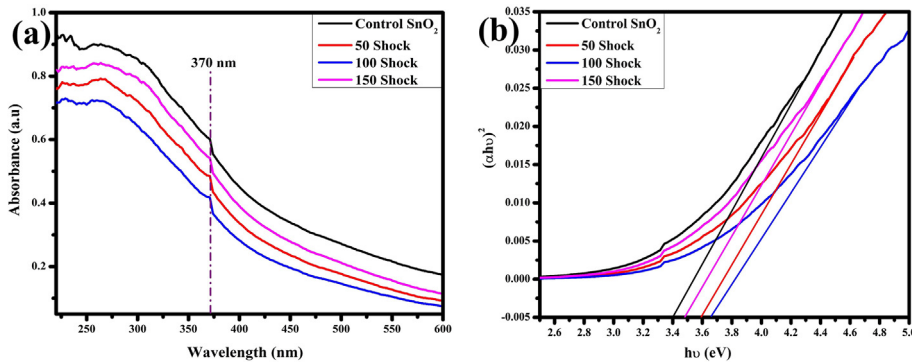

Figure 8. (a) UV absorption spectrum and (b) Tauc plot of control SnO$_2$ and shock exposed SnO$_2$ NPs.

To understand more about the in-depth quantitative behavior of the SnO$_2$ NPs, the Bandgap energy of the control SnO$_2$ and shock exposed NPs were calculated from their absorption spectrum according to Eq. (7),

$$(\alpha h\nu) = A\left(h\nu - E_g\right)^n \tag{7}$$

where α is the absorption coefficient, h𝜈 is the energy of the photon, Eg is Band Gap energy, a is constant, and n is the nature of the semiconductor whether it is a direct transition (n = 1/2) or indirect transition (n = 2). Generally SnO$_2$ direct Bandgap cassiterite (ore of tin) semiconducting material. The control SnO$_2$ NPs show the Bandgap of 3.40 eV. Whereas the shock treated SnO$_2$ NPs show the Bandgap of 3.59 eV, 3.66 eV, and 3.48 eV for 50 shocks, 100 shocks, and 150 shocks, shown in Figure (8)b. The variation of band gap may be due to the defects created during the propagation of the shock waves. In addition to that, the change in particle size plays a vital role in the band gap. The size of the test samples are 30

nm, 26 nm, 33 nm and 30 nm for control, 50, 100 and 150 shocked conditions, respectively, which clearly reflects on the band gap value changes. These results clearly reveal that the band gap energy can be tuned precisely, which is why it is used as a semiconducting material for many applications.

3.6. Photoluminescence study

Figure (9) Shows the PL spectra for the SnO$_2$ NPs; the emission peak at 330 nm is due to the self-internal recombination of the charged carriers. The broad peak in the region from 590-615 nm indicates the defects in the SnO$_2$ NPs [56]. Control SnO$_2$ and shock treated NPs show the intensity peak in the same region. Among these, 50 shocks show higher intensity peaks due to the small internal stress value between Sn–O. Therefore, the recombination rate will increase. Generally, higher bond length between Sn–O creates a higher intensity peak. 100,150 shocks
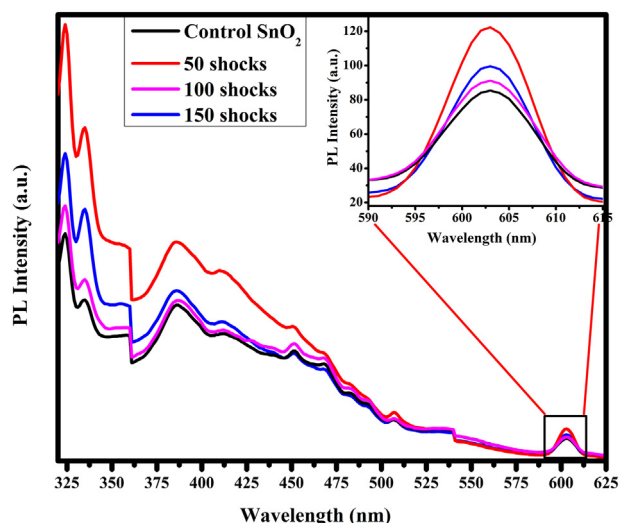
Figure 9. PL spectra for the control SnO₂ and shock exposed SnO₂ NPs.

SnO₂ NPs disclose lower intensity peaks, demonstrating that the bond length is affected during the impulsion of shocks. Thus, the oxygen vacancies are created in the structure [57]. Reduction of intensity peak can also occur between surface area and concentration volume of oxygen vacancies.

### 3.7. Photocatalytic activity and degradation mechanism of SnO₂ NPs

The control SnO₂ and shock exposed samples demonstrate different Bandgap and PL intensity. Based on varying intensities, the catalytic efficiency of the SnO₂ NPs varies. The control SnO₂ NPs exhibit the highest efficiency of 96% within 90 min. This is due to the defect-free structure of

SnO₂ NPs at control conditions. The 50 shock, 100 shocks, 150 shocks exposed SnO₂ NPs display the lowest efficiency of 74%, 92%, 86% compared to control SnO₂ NPs within 90 min, as shown in Figure (10).The low efficiency due to the particle interaction during the shock treatment creates structural defects; these defects act as the recombination center for e- and h⁺. When the shock impulsion is applied, structural deformation like stress and strain occurs and influences the photocatalytic property. From the USDM studies, the stain value calculated 1.1446 (50 shocks), 1.5933 (100 shocks), and 0.7602 (150 shocks). Increasing strain value causes a blue shift in the absorption peak; accordingly, the Bandgap value also changes [58, 59].

Figure (11) Shows the efficiency and kinetics graphs of SnO₂ NPs. Kinetics study also reveals that correlation coefficient value (r^2) for control SnO₂, 50 shocks, 100 shocks, and 150 shocks SnO₂ NPs exhibits the pseudo-first-order kinetics values of 0.9779, 0.9377, 0.9724, and 0.9904 while the second-order kinetic values of 0.6472, 0.7689, 0.7648, and 0.8728. This will clearly show the control SnO₂ and shock exposed NPs follows the first-order reaction, shown in Table (3).

The photocatalytic activity test was carried under UV light due to the wide band of the SnO₂ NPs. Under UV light (376 nm) irradiation the following reaction takes place in SnO₂ NPs, Mechanism of SnO₂ NPs VB dye degradation shown in Figure (12).

(i) When the UV light penetrates the photocatalyst the electrons (e-) get excited from the valence band to the conduction band due to the higher photon energy of UV light compared to SnO₂ band gap energy (Eq. (8)).

$$SnO_2 + h\nu \,(UV\,Light) \rightarrow SnO_2\left(h_{vb}^+ + e_{cb}^-\right) \tag{8}$$
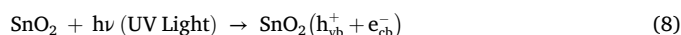
(ii) Conduction band reaction: Excited electrons will react with oxygen molecules (O₂) to form superoxide anions (O₂⁻) (-0.33 vs
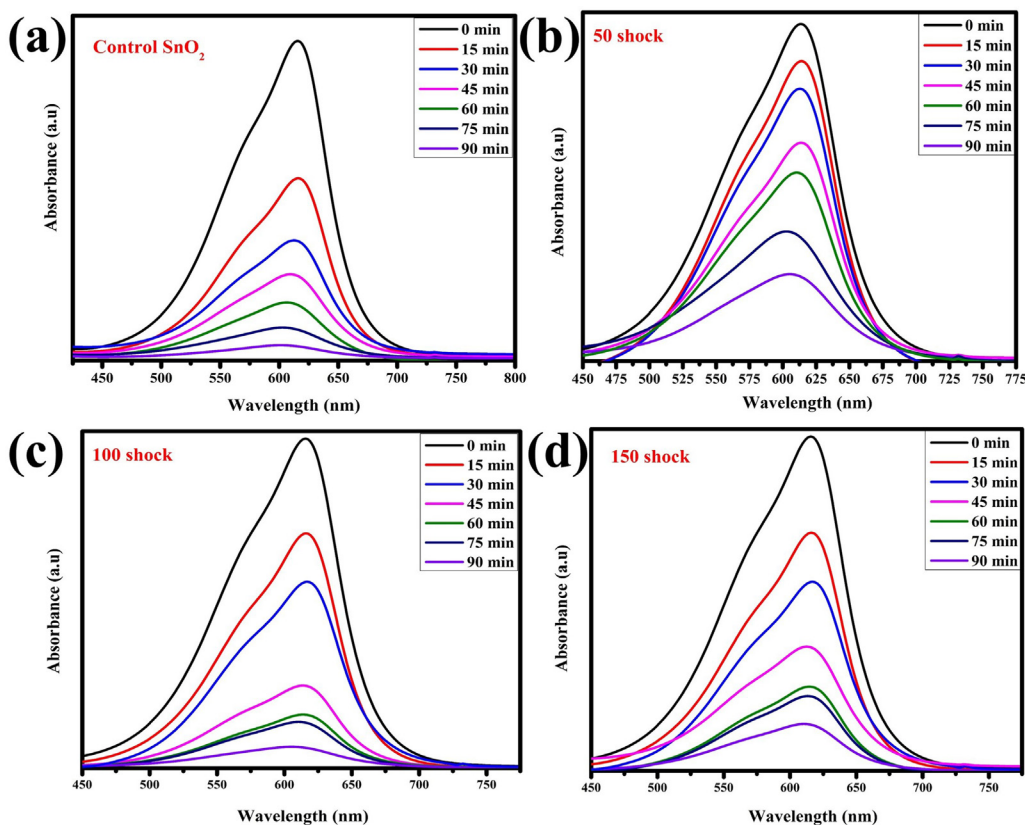

Figure 10. (a) control SnO₂, (b) 50 shocks, (c) 100 shocks, and (d) 150 shocks VB dye degradation.
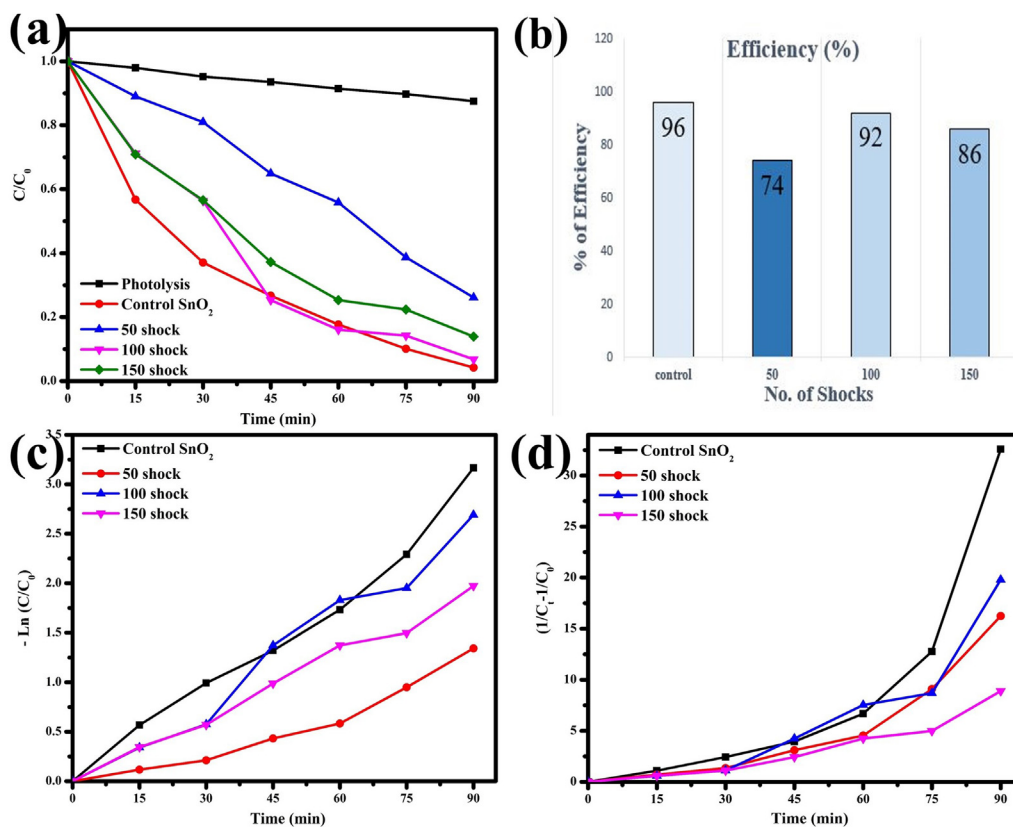
Figure 11. (a) & (b) Efficiency graphs, (c) Pseudo first, and (d) second order kinetics graphs.

Table 3. Efficiency and kinetics values of control SnO$_2$ and shock exposed SnO$_2$ NPs.

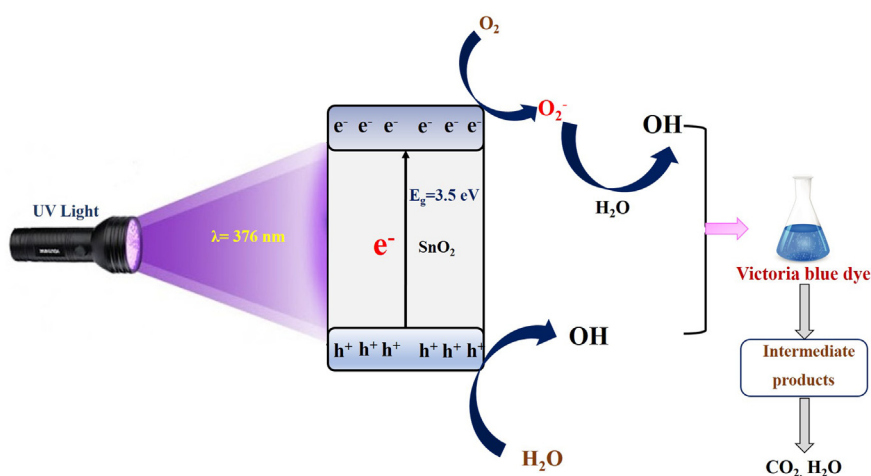| Sr.No	Samples	Degradation efficiency (%)	Victoria blue (VB)				
			First order model			Second order model	
			Rate constant (min^{-1})	r^2		Rate constant (min^{-1})	r^2
1.	control SnO$_2$	96	0.0322	0.9779		0.2226	0.6472
2.	50 shock	74	0.0144	0.9377		0.1273	0.7689
3.	100 shock	92	0.0284	0.9724		0.1523	0.7648
4.	150 shock	86	0.0214	0.9904		0.0772	0.8728

Figure 12. Mechanism of SnO$_2$ NPs VB dye degradation.

NHE). These superoxide ions react with dye molecules to form intermediate products with water (Eqs. (9), (10)).

$$e_{cb}^- + O_2 \rightarrow O_{2-} \qquad (9)$$

$$O_{2-} + VB\ dye \rightarrow Intermediates + water \qquad (10)$$
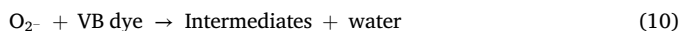
(iii) Valence band reaction: Holes will react with water molecules (H_2O) to form a hydroxyl radical (OH^-) (+2.33 vs NHE). These hydroxyls have enough power to break the dye molecules' chemical structure to form an intermediate with water (Eqs. (11), (12)).

$$H_2O \rightarrow H^+ + OH^- \qquad (11)$$

$$OH^- + VB\ dye \rightarrow Intermediates + water \qquad (12)$$

4. Conclusion

SnO_2 nanoparticles were successfully synthesized by a toxic free green microwave-assisted hydrothermal method and then the green synthesized nanoparticles were treated with 50, 100, and 150 shock pulses. The powder XRD characterization confirmed that SnO_2 nanoparticles belong to a tetragonal structure and confirmed its highly crystalline and stabilized structure under the impulsion of shock conditions. From Rietveld refinement profile analysis study, it is evident that the photocatalytic efficiency in degrading VB dye under UV light is higher in the control SnO_2 NPs than the shock treated samples. This may be due to the changes in the bond length and other parameters like stress, strain, etc., which is confirmed by the W–H plot. FTIR exhibits high molecular stabilized SnO_2 nanoparticles. FESEM images are clearly evident for the morphology of SnO_2 nanoparticles did not change, only the particle size was changed. Control, 50, 100, and 150 shocks treated SnO_2 nanoparticles show a stable optical property.

Declarations

Author contribution statement

M. Jarvin: Conceived and designed the experiments; Performed the experiments; Wrote the paper.

S. S. R. Inbanathan, S. A. Martin Britto Dhas: Analyzed and interpreted the data; Wrote the paper.

D. Rani Rosaline: Contributed reagents, materials, analysis tools or data.

A. Josephine Prabha: Performed the experiments.

Data availability statement

Data will be made available on request.

Declaration of interests statement

The authors declare no conflict of interest.

Additional information

No additional information is available for this paper.

References

[1] Y.H. Chiu, T.F.M. Chang, C.Y. Chen, M. Sone, Y.J. Hsu, Mechanistic insights into photodegradation of organic dyes using heterostructure photocatalysts, Catalysts 9 (5) (2019) 430.

[2] S.K. Panda, I. Aggarwal, H. Kumar, L. Prasad, A. Kumar, A. Sharma, V. Mishra, Magnetite nanoparticles as sorbents for dye removal: a review, Environ. Chem. Lett. (2021) 1–39.

[3] S. Benkhaya, S. M'rabet, A.E. Harfi, Classifications, properties, recent synthesis and applications of azo dyes, Heliyon 6 (1) (2020) 3271.

[4] T.S. Anirudhan, P.L. Divya, J. Nima, S. Sandeep, Synthesis and evaluation of Iron-doped titania/silane based hydrogel for the adsorptional photocatalytic degradation of Victoria blue under visible light, J. Colloid Interface Sci. 434 (2014) 48–58.

[5] S.P. Kim, M.Y. Choi, H.C. Choi, Photocatalytic activity of SnO_2 nanoparticles in methylene blue degradation, Mater. Res. Bull. 74 (2016) 85–89.

[6] G. Elango, S.M. Roopan, Efficacy of SnO_2 nanoparticles toward photocatalytic degradation of methylene blue dye, J. Photochem. Photobiol. B Biol. 155 (2016) 34–38.

[7] V. Paramarta, A. Taufik, L. Munisa, R. Saleh, Sono-and photocatalytic activities of SnO_2 nanoparticles for degradation of cationic and anionic dyes, in: AIP Conference Proceedings, 1788, AIP Publishing LLC, 2017, January, p. 30125. No. 1.

[8] Y. Li, Q. Yang, Z. Wang, G. Wang, B. Zhang, Q. Zhang, D. Yang, Rapid fabrication of SnO_2 nanoparticle photocatalyst: computational understanding and photocatalytic degradation of organic dye, Inorg. Chem. Front. 5 (12) (2018) 3005–3014.

[9] N. Srivastava, M. Mukhopadhyay, Biosynthesis of SnO_2 nanoparticles using bacterium Erwinia herbicola and their photocatalytic activity for degradation of dyes, Ind. Eng. Chem. Res. 53 (36) (2014) 13971–13979.

[10] P.V. Viet, C.M. Thi, L.V. Hieu, The high photocatalytic activity of SnO_2 nanoparticles synthesized by hydrothermal method, J. Nanomater. (2016).

[11] T.B. Devi, S. Begum, M. Ahmaruzzaman, Photo-catalytic activity of Plasmonic Ag@ AgCl nanoparticles (synthesized via a green route) for the effective degradation of Victoria Blue B from aqueous phase, J. Photochem. Photobiol. B Biol. 160 (2016) 260–270.

[12] M.V. Arularasu, M. Anbarasu, S. Poovaragan, R. Sundaram, K. Kanimozhi, C.M. Magdalane, M. Maaza, Structural, optical, morphological and microbial studies on SnO_2 nanoparticles prepared by co-precipitation method, J. Nanosci. Nanotechnol. 18 (5) (2018) 3511–3517.

[13] A.M. El-Rafei, H. Youssef, N.M. Ahmed, Synthesis and characterization of nano-/micro-crystalline SnO using microwave and hydrothermal techniques, J. Ceram. Sci. Technol. 5 (3) (2014) 217–222.

[14] S. Suthakaran, S. Dhanapandian, N. Krishnakumar, N. Ponpandian, Hydrothermal synthesis of SnO_2 nanoparticles and its photocatalytic degradation of methyl violet and electrochemical performance, Mater. Res. Express 6 (8) (2019) 850i3.

[15] M.A.M. Akhir, S.A. Rezan, K. Mohamed, M.M. Arafat, A.S.M.A. Haseeb, H.L. Lee, Synthesis of SnO_2 nanoparticles via hydrothermal method and their gas sensing applications for ethylene detection, Mater. Today Proc. 17 (2019) 810–819.

[16] T. Krishnakumar, N. Pinna, K.P. Kumari, K. Perumal, R. Jayaprakash, Microwave-assisted synthesis and characterization of tin oxide nanoparticles, Mater. Lett. 62 (19) (2008) 3437–3440.

[17] A.K. Singh, U.T. Nakate, Microwave Synthesis, Characterization and Photocatalytic Properties of SnO2 Nanoparticles, 2013.

[18] J. Zhang, L. Gao, Synthesis of SnO_2 nanoparticles by the sol-gel method from granulated tin, Chem. Lett. 32 (5) (2003) 458–459.

[19] M. Aziz, S.S. Abbas, W.R.W. Baharom, Size-controlled synthesis of SnO_2 nanoparticles by sol-gel method, Mater. Lett. 91 (2013) 31–34.

[20] S. Gnanam, V. Rajendran, Synthesis of tin oxide nanoparticles by sol–gel process: effect of solvents on the optical properties, J. Sol. Gel Sci. Technol. 53 (3) (2010) 555–559.

[21] K. Balakrishnan, N. Murugasean, Synthesis and characterization of SnO2 nanoparticles by co-precipitation method, Int. J. Nano Dimens. (IJND) 12 (1) (2021) 76–82.

[22] S. Naz, I. Javid, S. Konwar, K. Surana, P.K. Singh, M. Sahni, B. Bhattacharya, A simple low cost method for synthesis of SnO_2 nanoparticles and its characterization, SN Appl. Sci. 2 (5) (2020) 1–8.

[23] P. Sarabadani, M. Sadeghi, M. Ghasemi, Z. Asadollahi, N. Afshari, Synthesis and characterization of tin oxide nanoparticles by solid state chemical reaction method, J. Cluster Sci. 22 (2) (2011) 131–140.

[24] V. Garg, H. Sharma, D. Rehani, R. Kumari, V. Kumar, M.K. Tiwari, M. Saxena, Synthesis and Characterization of Temperature Controlled SnO_2 Nanoparticles by Solid-State Reaction Method, 2020.

[25] K.C. Suresh, S. Surendhiran, P.M. Kumar, E.R. Kumar, Y.S. Khadar, A. Balamurugan, Green synthesis of SnO_2 nanoparticles using Delonix elata leaf extract: evaluation of its structural, optical, morphological and photocatalytic properties, SN Appl. Sci. 2 (10) (2020) 1–13.

[26] E. Haritha, S.M. Roopan, G. Madhavi, G. Elango, N.A. Al-Dhabi, M.V. Arasu, Green chemical approach towards the synthesis of SnO_2 NPs in argument with photocatalytic degradation of diazo dye and its kinetic studies, J. Photochem. Photobiol. B Biol. 162 (2016) 441–447.

[27] G. Elango, S.M. Kumaran, S.S. Kumar, S. Muthuraja, S.M. Roopan, Green synthesis of SnO_2 nanoparticles and its photocatalytic activity of phenolsulfonphthalein dye, Spectrochim. Acta Mol. Biomol. Spectrosc. 145 (2015) 176–180.

[28] S. Haq, W. Rehman, M. Waseem, A. Shah, A.R. Khan, M.U. Rehman, G. Ali, Green synthesis and characterization of tin dioxide nanoparticles for photocatalytic and antimicrobial studies, Mater. Res. Express 7 (2) (2020) 25012.

[29] P.S.S. Selvam, D. Ganesan, V. Rajangam, A. Raji, V. Kandan, Green synthesis of SnO$_2$ nanoparticles for catalytic degradation of rhodamine B, Iran. J. Sci. Technol. Trans. A-Science 44 (3) (2020) 661–676.

[30] P. Boroojerdian, Microwave–assisted hydrothermal synthesis and optical characterization of SnO$_2$ nanoparticles, Int. J. Nanosci. Nanotechnol. 9 (3) (2013) 139–142.

[31] J.P. Gonjal, E. Morán, R. Schmid, Microwaves: microwave assisted hydrothermal synthesis of nanoparticles, J. Nanotechnol. (2015) 561–570.

[32] S.K. Tripathy, A. Mishra, S.K. Jha, R. Wahab, A.A. Al-Khedhairy, Microwave assisted hydrothermal synthesis of mesoporous SnO$_2$ nanoparticles for ethanol sensing and degradation, J. Mater. Sci. Mater. Electron. 24 (6) (2013) 2082–2090.

[33] Z.W. Han, S. Xu, L.F. Xie, Y.C. Han, Study on the application of emulsion explosives in synthesizing nanostructured ceria, Combust. Explos. Shock Waves 50 (4) (2014) 477–482.

[34] A.W. Dean, W.F. Heard, C.M. Loeffler, B.E. Martin, X. Nie, A new Kolsky bar dynamic spall technique for brittle materials, J. Dynam. Behav. Mater. 2 (2) (2016) 246–250.

[35] A. Sivakumar, C. Victor, M.M. Nayak, S.M.B. Dhas, Structural, optical, and morphological stability of ZnO nano rods under shock wave loading conditions, Mater. Res. Express 6 (4) (2019) 45031.

[36] A. Sivakumar, S. Kalaiarasi, S.S.J. Dhas, A.I. Almansour, R.S. Kumar, N. Arumugam, S.M.B. Dhas, Assessment of shock wave resistance on brookite TiO$_2$, J. Mater. Sci. Mater. Electron. (2021) 1–9.

[37] A. Singhal, A. Gupta, Sustainable synthesis of silver nanoparticles using exposed X-ray sheets and forest-industrial waste biomass: assessment of kinetic and catalytic properties for degradation of toxic dyes mixture, J. Environ. Manag. 247 (2019) 698–711.

[38] A. Rita, A. Sivakumar, S.M.B. Dhas, Investigation of structural and magnetic phase behaviour of nickel oxide nanoparticles under shock wave recovery experiment, J. Supercond. Nov. Magnetism 33 (6) (2020) 1845–1849.

[39] A.B. Garg, Pressure-induced volume anomaly and structural phase transition in nanocrystalline SnO$_2$, Phys. Status Solidi 251 (7) (2014) 1380–1385.

[40] H.T. Girão, T. Cornier, S. Daniele, R. Debord, M.A. Caravaca, R.A. Casali, D. Machon, Pressure-induced disordering in SnO$_2$ nanoparticles, J. Phys. Chem. C 121 (28) (2017) 15463–15471.

[41] M. Reto, M.E. Figueira, H.M. Filipe, C.M. Almeida, Chemical composition of green tea (Camellia sinensis) infusions commercialized in Portugal, Plant Foods Hum. Nutr. 62 (4) (2007) 139–144.

[42] J.C. Selvakumari, M. Ahila, M. Malligavathy, D.P. Padiyan, Structural, morphological, and optical properties of tin (IV) oxide nanoparticles synthesized using Camellia sinensis extract: a green approach, Int. J. Miner. Metal. Mater. 24 (9) (2017) 1043–1051.

[43] M.R. Samarghandi, M. Zarrabi, A. Amrane, M.N. Sepehr, M. Noroozi, S. Namdari, A. Zarei, Kinetic of degradation of two azo dyes from aqueous solutions by zero iron powder: determination of the optimal conditions, Desalination Water Treat. 40 (1-3) (2012) 137–143.

[44] A. Rita, A. Sivakumar, S.S.J. Dhas, S.M.B. Dhas, Structural, optical and magnetic properties of silver oxide (AgO) nanoparticles at shocked conditions, J. Nanostruct. Chem. 10 (4) (2020) 309–316.

[45] P. Muhammed Shafi, A. Chandra Bose, Impact of crystalline defects and size on X-ray line broadening: a phenomenological approach for tetragonal SnO$_2$ nanocrystals, AIP Adv. 5 (5) (2015) 57137.

[46] S. Yousefi, B. Ghasemi, M.P. Nikolova, Morpho/Opto-structural characterizations and XRD-assisted estimation of crystallite size and strain in MgO nanoparticles by applying Williamson–Hall and size–strain techniques, J. Cluster Sci. (2021) 1–11.

[47] K. Maniammal, G. Madhu, V. Biju, X-ray diffraction line profile analysis of nanostructured nickel oxide: shape factor and convolution of crystallite size and microstrain contributions, Phys. E Low-dimens. Syst. Nanostruct. 85 (2017) 214–222.

[48] M.A. Brza, S.B. Aziz, H. Anuar, F. Ali, E.M. Dannoun, S.J. Mohammed, S. Al-Zangana, Tea from the drinking to the synthesis of metal complexes and fabrication of PVA based polymer composites with controlled optical band gap, Sci. Rep. 10 (1) (2020) 1–17.

[49] P.A. Luque, O. Nava, C.A. Soto-Robles, M.J. Chinchillas-Chinchillas, H.E. Garrafa-Galvez, Y.A. Baez-Lopez, A. Castro-Beltrán, Improved photocatalytic efficiency of SnO$_2$ nanoparticles through green synthesis, Optik 206 (2020) 164299.

[50] L.C. Nehru, C. Sanjeeviraja, Rapid synthesis of nanocrystalline SnO$_2$ by a microwave-assisted combustion method, J. Adv. Ceram. C 3 (3) (2014) 171–176.

[51] W.B. Soltan, M.S. Lassoued, S. Ammar, T. Toupance, Vanadium doped SnO$_2$ nanoparticles for photocatalytic degradation of methylene blue, J. Mater. Sci. Mater. Electron. 28 (21) (2017) 15826–15834.

[52] A. Azam, S.S. Habib, N.A. Salah, F. Ahmed, Microwave-assisted synthesis of SnO2 nanorods for oxygen gas sensing at room temperature, Int. J. Nanomed. 8 (2013) 3875.

[53] E. Abdelkader, L. Nadjia, B. Ahmed, Preparation and characterization of novel CuBi$_2$O$_4$/SnO$_2$ p–n heterojunction with enhanced photocatalytic performance under UVA light irradiation, J. King Saud Univ. Sci. 27 (1) (2015) 76–91.

[54] J. Mayandi, M. Marikkannan, V. Ragavendran, P. Jayabal, Hydrothermally synthesized Sb and Zn doped SnO$_2$ nanoparticles, J. Nanosci. Nanotechnol. 2 (2014) 707–710.

[55] A. Radoń, A. Drygała, Ł. Hawełek, D. Łukowiec, Structure and optical properties of Fe$_3$O$_4$ nanoparticles synthesized by co-precipitation method with different organic modifiers, Mater. Char. 131 (2017) 148–156.

[56] P. Van Tuan, V.T. Tan, T.T. Phuong, H.T.T. Quỳnh, T.N. Khiem, The dependence of morphology, structure, and photocatalytic activity of SnO$_2$/rGO nanocomposites on hydrothermal temperature, Mater. Res. Express 6 (10) (2019) 106204.

[57] L.C. Nehru, V. Swaminathan, C. Sanjeeviraja, Photoluminescence studies on nanocrystalline tin oxide powder for optoelectronic devices, Am. J. Mater. Sci. 2 (2) (2012) 6–10.

[58] L. Lv, Y. Shen, X. Gao, J. Liu, S. Wu, Y. Ma, Z. Zhou, Strain engineering on the electrical properties and photocatalytic activity in gold sulfide monolayer, Appl. Surf. Sci. 546 (2021) 149066.

[59] H. Ennaceri, M. Boujnah, D. Erfurt, J. Rappich, X. Lifei, A. Khaldoun, A. Taleb, Influence of stress on the photocatalytic properties of sprayed ZnO thin films, Sol. Energy Mater. Sol. Cell. 201 (2019) 110058.